2010 TOPCO 崇越論文大賞

論文題目：

Applying nanoparticles to develop advanced antireflection techniques for Si solar cells

報名編號： SB0011

Abstract

In this study, we systematically investigated the phenomenon of light trapping in Si solar cells coated with metal (Au) and dielectric (TiO_2, SiO_2) nanoparticles (NPs). In contrast to previous reports, herein we propose that the photocurrent enhancement of solar cells should be attributed to the limited antireflection ability of the Au NPs arrays. In other words, the Au NP arrays might not enhance the absorption of the active layer in cells when no light was reflected from the air–substrate interface. Therefore, we replaced the Au NPs with dielectric NPs, which possess lower extinction coefficients, and then optimized the antireflection property of the TiO_2 NPs arrays. We used a simple, rapid, and cheap solution-based method to prepare close-packed TiO_2 NP films on Si solar cells; these devices exhibited a uniform and remarkable increase (ca. 30%) in their photocurrents. To the best of our knowledge, this uniform photocurrent enhancement is greater than those obtained from previously reported metal and dielectric NP–enhanced Si wafer-based solar cells.

Keywords: Metal and dielectric nanoparticles, Antireflective nanoparticles, Surface plasmon resonance, Si solar cells, Near field phenomenon

1. Introduction

The threat of an upcoming energy shortage is making it increasingly important to develop new substitute energy technologies. Although the current production of solar cells is dominated by crystalline silicon modules, because of their mature fabrication techniques and relatively high efficiency, the high refractive index of Si means that more than 40% of the incident light is reflected back, which greatly reduces the conversion efficiency of photovoltaic devices. Thus, light trapping has become an important aspect of increasing the efficiency of crystalline Si solar cells; several techniques have been developed, such as the use of antireflection-coating thin films and textured structures (Winderbaum et al., 1997; Nagel et al., 1999; Lee et al., 2002; Macdonald et al., 2004; Chen et al., 2007). Most techniques for texturing Si have focused on employing dry or wet etching processes, either in conjunction with a mask to achieve large, regular features or without a mask to produce much smaller, more-random features. Nevertheless, implementing most of these existing texturing techniques is too expensive and/or of too low reproducibility to make the development of solar cells truly economically competitive with fossil fuels.

In recent years, there has been increasing interest in the unique physical and chemical properties of metal nanostructures because of their fundamental and technological applications. For example, metal nanoparticles (NPs) are attractive for their surface plasmon resonance (SPR) properties. The strong interactions of metallic NPs with incident light originate from the excitation of collective oscillations of conduction electrons within these particles (Kelly et al., 2003). The SPR frequencies of metal NPs can be tuned through variations in their sizes, shapes, structures, aggregate morphologies, and surface chemistry and of the refractive index of the surrounding medium (Yguerabide, 1998; Caruso and Antonietti, 2001; Jackson and Halas 2001; Novak et al., 2001; Selvakannan and Sastry, 2005; Orendorff et al., 2006; Kubo et al., 2007). Thus, a new method for increasing the degree of light absorption in various solar cells is the use of SPR from noble metal NPs. For example, metal NPs embedded within organic and Si solar cells (Hallermann et al., 2008; Kim et al., 2008; Duche et al., 2009; Khurgin et al., 2009) or deposited on the front side of GaAs and Si solar cells featuring a buried p–n junction (Schaadt et al., 2005; Cole and Halas, 2006; Lim et al., 2007; Pillai et al., 2007; Matheu et al., 2008; Nakayamae et al., 2008; Sundararaian et al., 2008) have exhibited wavelength-dependent increases in their photocurrents. The observed increase in photocurrents from the embedded NPs can be attributed to improved light absorption in the active layer, due to the enhanced electromagnetic field in the vicinity of the NPs during SPR (Hallermann et al., 2008; Khurgin et al., 2009). Embedded, conductive metal NPs might, however, serve as electron–hole (e–h) pair recombination centers to suppress the efficiencies of solar cells.

To prepare NP-coated Si solar cells, Pillai et al. (2007) deposited Ag NPs onto planar wafer–based cells, achieving a ca. 19% increase in photocurrent. Lim et al. (2007) also reported experimental and simulated results for Au NPs positioned atop a Si photodiode, achieving a maximum photocurrent enhancement of ca. 3% (density: 3 particles μm^{-2}) at the SPR wavelength. Sundararaian et al. (2008) reported a study of the changes in localized photocurrent in a buried Si photodiode induced by various NPs: Au NPs, Au nanoshells, and nanoshell aggregates varying in diameter and SPR wavelength. Moreover, Catchpole et al. (2008) reported the design principles of SPR-enhanced Si solar cells, indicating that improved light absorption of cells derived mostly from the longer optical path lengths in the active layer, due to the forward scattered fields from the NPs. Notably, however, commercial wafer-based Si solar cells generally feature long absorbed optical paths and absorb strongly in the visible region; therefore, the longer optical path lengths induced by the scattered fields from metal NPs might not effectively enhance the photocurrents of wafer-based Si solar cells.

In this study, we investigated the phenomenon of absorption enhancement of the active layers in Si solar cells when metal and dielectric NPs were coated on the front sides of the cells. First, we used the three-dimensional finite-difference time domain (FDTD) method to analyze the optical behavior in the near field regime of a Si substrate having different surface coverages of Au NPs. Based on analyses of the total transmission and reflection, we further examined the functions of the Au NPs arrays. In particular, we were concerned with the change in the transmission power, because more transmitted light into the substrates increases the optical transition rate and, consequently, the e–h pair generation rate. In contrast to previous reports (Catchpole and Polman, 2008), herein we propose that the photocurrent enhancement of solar cells should be attributed to the limited antireflection ability of the Au NPs arrays. In other words, the Au NP arrays might not enhance the absorption of the active layer in cells when no light was reflected from the air–substrate interface. To verify this hypothesis, we tested a variety of low reflection conditions. As simulation models, we designed two well-known antireflection structures on Si substrates: a single layer Si_3N_4 film and a sub-wavelength pyramidal structure. In experiments, we measured the current density–voltage characteristics of a commercial textured Si solar cell featuring a Si_3N_4 antireflection coating. We also used a transverse magnetic (TM)–polarized light source under no-reflection conditions (at the so-called Brewster angle) and obtained photocurrents from a planar Si solar cell. The optical behavior of the Au NP arrays under these specific conditions is discussed in detail below. Finally, we used the FDTD method to investigate the optical behavior of the dielectric NP arrays deposited atop Si wafers and developed a simple, solution-based method for the preparation of NP antireflection layers on planar Si solar cells.

2. Experimental

Materials: All chemicals were used as received. Aqueous poly-l-lysine solution and ethanol (EtOH, 99.8%) were obtained from Acros. Titanium oxide colloid solution in xylene (TiO_2, 45–47%) was obtained from Aldrich. The crystalline TiO_2 dispersion (20% rutile, 80% anatase) was composed of particles having diameters of less than 100 nm (determined using dynamic light scattering); the primary particle size was ca. 15 nm. The gold colloid (D = 100 nm) was obtained from Ted Pella. The p-type Si wafers (100) were obtained from Summit-Tech. The commercial Si solar cells were obtained from Motech Industries.

Planar Si Solar Cells: Si p–n junction solar cells were fabricated from 6-inch-diameter, 600-μm-thick, p-type Si (100) wafers. To form the p–n junctions, P atoms were ion-implanted at 26 keV and then diffused into the wafers for 30 min at 800 °C under a N_2 atmosphere. Ohmic contacts to the n-type layer were formed in a finger pattern using 200-nm Al metallization in a standard lift-off process; a 300-nm Al film was employed to form a back contact to the p-type layer.

Au and TiO_2 NP Monolayers: For the deposition of Au NPs, Si cells were immersed for 10 min in an aqueous solution of poly-l-lysine. The cells were then rinsed thoroughly with ultrapure water (UPW) to remove any unbound polymers from the surface. Next, the cells were immersed for 1 h in vials containing the Au NPs. The Au NP–deposited cells were then spun at 3000 rpm to remove any excess NPs. After performing a final UPW rinse, the samples were dried and stored under ambient conditions until required for further use. For deposition of the TiO_2 NPs, the TiO_2 solution was diluted to 4.68 wt% with EtOH and then spun onto the clean Si substrates at various spinning rates. The samples were then stored under ambient conditions until required for further use.

Characterization: The active area of the cells was fixed at 3 cm^{-2}. Photocurrent spectra of these devices were obtained using a Xe lamp with (or without) a TM-polarized filter as an illumination source and a grating monochromator with a 1200 groove/mm grating, yielding monochromatic light for measurements extending over the wavelength range 400–850 nm. Current density–voltage (J–V) characteristics were obtained under illumination from a Xe lamp with a global AM 1.5 filter, using a room-temperature probe station and a Keithley 2400 semiconductor parameter analyzer. The reflectance spectra were measured using a Hitachi U4100 optical spectrometer. The NP-deposited substrates were observed using a JEOL JSM-6500F scanning electron microscope. The three-dimensional FDTD method was used to analyze the optical behavior in the near field regime of monolayer NP arrays deposited on Si substrates with various surface coverages. The surface coverage and volume fraction were defined using the expressions $\frac{N \times \pi r^2}{Area_{simulation}}$ and $\frac{N \times {}^4\!/_3 \pi r^3}{2r \times Area_{simulation}}$, respectively, where N is the sum of the particles in the simulation area, $Area_{\mathrm{simulation}}$ was fixed at 1 μm × 1 μm, and r is the radius of the particles.

3. Results and Discussion

In previous investigations, we used the three-dimensional FDTD method to analyze the antireflective ability of regular or randomly textured surfaces of Si substrates (Chen et al., 2007; Wan et al., 2008). In this study, we used the FDTD method to analyze the optical behavior of light propagating within the near-field regime on the surface of a Si substrate presenting different surface coverages of Au NPs. Figure 1 displays a typical model of a random-dispersed monolayer Au NP array [average diameter (*D*): 100 nm] directly in contact with a semi-infinite Si substrate. The optical constants of Au and Si substrate were obtained from the literature (Palik, 1985). In Figure 1b, S represents a light source propagating from 200 nm above the air–Si interface to the Si surface, R represents a monitor that integrates the time-averaged light power flowing through the plane at 300 nm above the air–Si interface, and T represents a monitor that integrates the time-averaged light power flowing through the plane at 50 nm beneath the air–Si interface. Because the incident plane wave from the light source was propagating only onto Si substrate, the integrated power from the R monitor represents the total reflected light (reflection); in contrast, the T monitor measured the total transmitted light (transmission) into the Si substrate, although this light had passed through a thin (50 nm) Si layer.

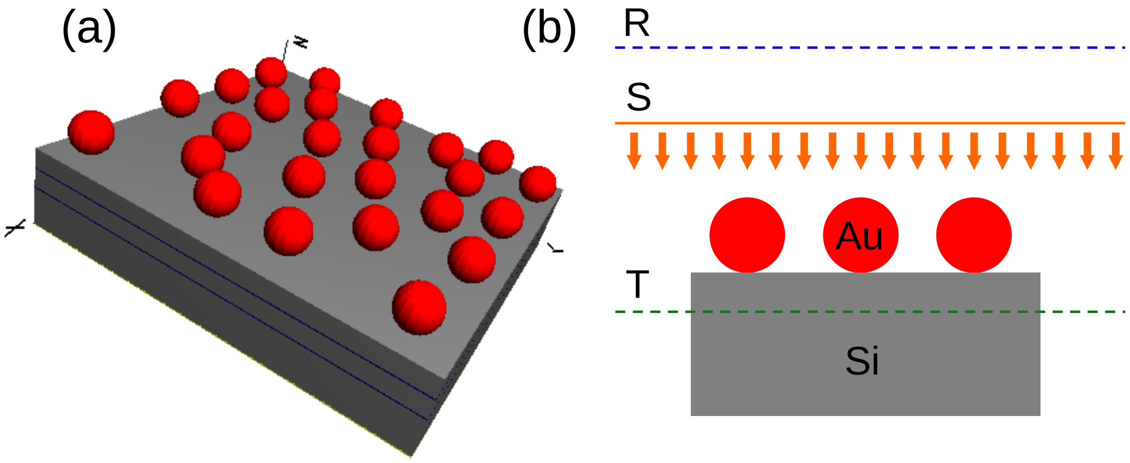

Figure 1. 3D model of a randomly dispersed Au NP array deposited on a Si substrate.

For convenience, we normalized the incident light power to unity. Figure 2 presents the results calculated for different surface coverages of Au NPs (0–62.8%) atop Si substrates. In Figure 2a, we observe two distinct features: the total transmission power increased at longer wavelengths after increasing the surface coverage of Au NPs, whereas it decreased dramatically at wavelengths less than 550 nm. Moreover, Figure

2b displays the total transmission powers of the Si substrates featuring different surface coverages of Au NPs, normalized with respect to the transmission power of the Si substrate in the absence of any Au NPs. The normalized transmission peaks were enhanced from 1.08 (λ = 650 nm; black line in Figure 2b) to 1.38 (λ = 700 nm; yellow line in Figure 2b) when the surface coverage of Au NPs increased from 3.9 to 39.3%. When we increased the surface coverage further to 62.8%, the peak intensity decreased slightly to 1.30 (λ = 750 nm; navy line in Figure 2b). In addition, the peaks underwent an obvious red shift (from 650 to 750 nm) upon increasing the surface coverage of Au NPs; presumably because of a coupling effect caused by the neighboring Au NPs (Khlebtsov et al., 2008). These findings indicate that more incident light could propagate into the Si substrate after positioning a Au NP array on the surface. The greater amount of transmitted light led to an increase in the e–h pair generation rate. Most importantly, the total transmission power obtained from our simulations represented the integrated time-averaged power of the light waves arriving at the monitor plane located only 50 nm below the air–Si interface. In other words, in our case, the effect of a longer light propagating path length was negligible and could be excluded. Nevertheless, our simulated results still featured wavelength-dependent increases in transmission, consistent with previous reports (Schaadt et al., 2005; Lim et al., 2007). We suspected that the increases in transmission might be attributable to reduced reflection of the Si substrates after depositing the Au NPs. Figure 2c displays the total reflection powers of Si substrates featuring various Au surface coverages. Upon increasing the Au surface coverage from 0 to 31.4%, the reflection power decreased dramatically over the entire wavelength regime, with an apparent dip at ca. 550 nm. The lowest value of reflection decreased from 0.34 to merely 0.008 after increasing the Au surface coverage to 31.4% (λ = 600 nm; yellow line in Figure 2c). In this case, we attribute the observably suppressed reflection over the entire wavelength regime to two reasons: (i) the intrinsic absorption of Au NPs at SPR wavelengths (Hagglund et al., 2008; Akimov et al., 2009) and (ii) forward scattering from the Au NPs into the Si substrates (Lim et al., 2007; Pillai et al., 2007). Note that the apparent dip ($\lambda < 550$ nm) in the transmission power curve in Figure 2a was also more strongly pronounced upon increasing the Au surface coverage from 0 to 31.4%. Based on the dips at shorter wavelengths in both the transmission and reflection spectra, we believe that the intrinsic absorption of the Au NPs had an apparently negative impact on the rate of generation of e–h pairs. Notably, the unavoidable absorption peak was close to the maximum power of the AM 1.5 solar spectrum (Cole and Halas, 2006). The suppressed reflection at longer wavelengths would, however, lead directly to an increase in transmission, as indicated in Figures 2a and 2c. In other words, the Au NP arrays act as defective antireflective coatings: they could reduce the amount of reflected light, scattering it to the Si substrate, while strongly absorbing the incident light at SPR wavelengths. We also noted increases in reflection (e.g., from 0.008 to 0.34 at 600 nm) upon further increasing the Au surface coverage from 31.4 to 62.8% (Figure 2c). This phenomenon might be attributable to more backward scattering of the metal NPs upon increasing their surface coverage (Pillai et al., 2007). In fact, when we deposited the Au NPs into a close-packed array (not shown), the optical behavior of the Au NP array was similar with that of a highly reflective metal layer. Furthermore, we also determined the average values for the reflection and transmission powers over wavelengths from 450 to 850 nm (Figure 2d). The average reflection initially decreased but then increased upon raising the surface coverage from 0 to 62.8%; in contrast, the average transmission followed a disproportional trend. These relationships supported our hypothesis that suppressed reflection induced the increases in transmission. Interestingly, the average reflection decreased by ca. 0.3 after coating with the Au NPs at a coverage of 31.4%, whereas the average transmission increased by only ca. 0.1 under the same conditions. Again, this behavior indicates that the Au NPs absorbed a portion of the incident light.

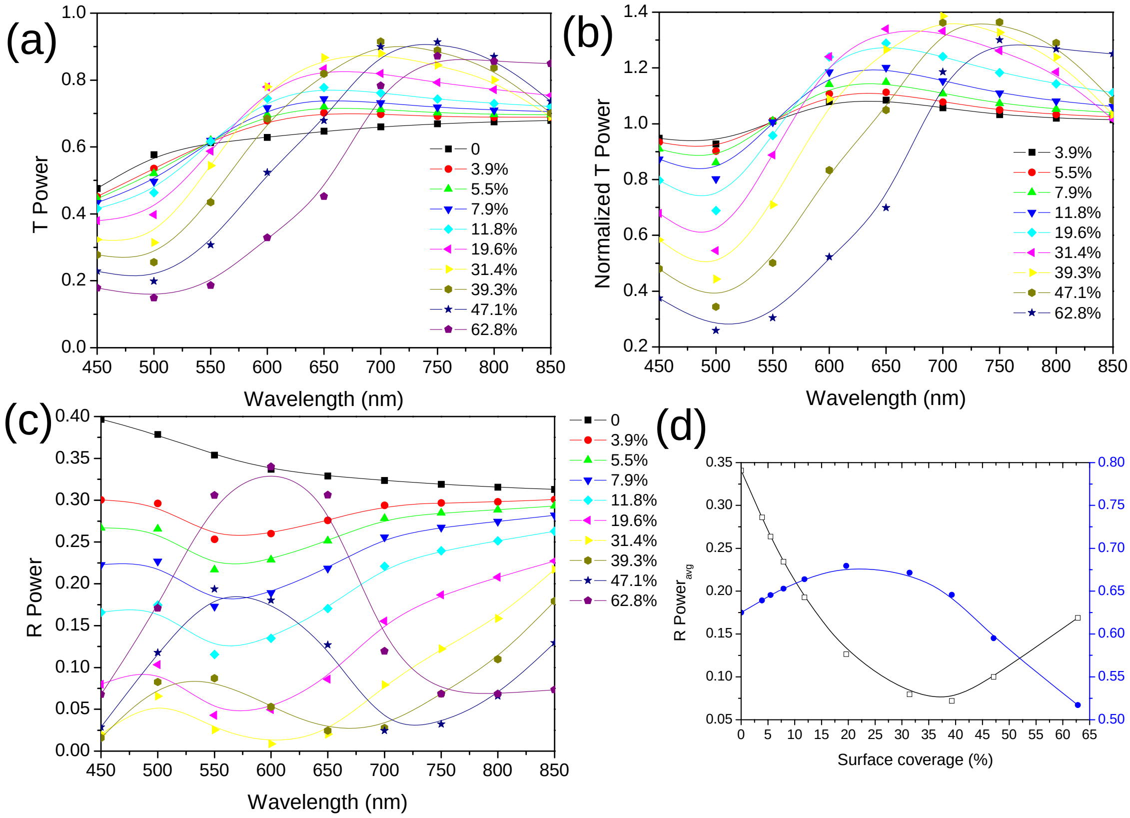

Figure 2. Calculated (a) transmission, (b) normalized transmission, and (c) reflection spectra of Si substrates presenting various surface coverages of Au NPs. (d) Average reflection (square) and transmission (circle) spectra obtained at various Au NP surface coverages.

Figure 3 displays the behavior of a plane wave (λ = 600 nm) propagating from 200 nm above the air–Si interface to the Si surface in the absence and presence of Au NPs. The light that reflected from the air–Si interface contributed entirely to the electric field at values of *Z* greater than 200 nm. Figure 3a displays the plane wave that propagated to the air–Si surface in the absence of Au NPs; an apparent reflection electric field existed above the Si surface. Figure 3b reveals that only a weak reflection field existed when the plane wave propagated to the Au NP array at a coverage of 31.4 %; most of the propagating wave was strongly scattered and distributed in the Si substrate. After increasing the Au surface coverage to 62.8%, however, the wave was strongly reflected into air, due to backward scattering from the Au NPs (Figure 3c). Therefore, the amount of reflected light in the near field decreased dramatically when the Au NP array had the optimized surface coverage of 31.4%. To further investigate the optical behavior of the transmitted plane wave, Figures 3d–f display the electric field distributions of the *X*–*Y* planes at a value of *Z* of –50 nm, corresponding to the models used in Figures 3a–c, respectively. Relative to the homogeneously distributed electric field in the Si substrate in the absence of Au NPs (Figure 3d), Figure 3e reveals a randomly distributed, distinctively brighter image at a Au NP coverage of 31.4%, indicating that a stronger electric field of the propagating plane wave existed at this *X*–*Y* plane and could induce greater rates of generation of e–h pairs. In contrast, Figure 3f reveals a randomly distributed, much darker image recorded at a Au NP coverage of 62.8%, presumably because the plane waves were strongly reflected and absorbed by the Au NPs at this higher surface coverage before they could propagate into the substrate.

Based on the FDTD simulations of the Si substrates coated with Au NP arrays at various surface coverages, we suspected that the Au NP arrays acted as absorbed antireflection coating layers. To verify this hypothesis, we analyzed the optical behavior of deposited Au NP arrays on two kinds of low-reflective Si structures: a single-layer antireflection coating (Si_3N_4) and a subwavelength-textured surface. Figure 4a presents a schematic representation of the deposited Au NP array on a Si_3N_4 (thickness: 65 nm)/Si substrate; Figures 4b and 4c display the reflection and transmission spectra of the Si_3N_4 coating on the Si substrate in presence and absence of the Au NP array (coverage: 19.6%), respectively. As expected, the single layer of Si_3N_4 effectively reduced the reflection of the Si wafer as a result of destructive interference (green line in Figure 4b) (Nagel et al., 1999), especially at a specific wavelength (the reflection power was 0.01 at 600 nm). The suppressed reflected light propagated into the Si substrate, leading to an obvious increase in the transmission power (green line in Figure 4c).

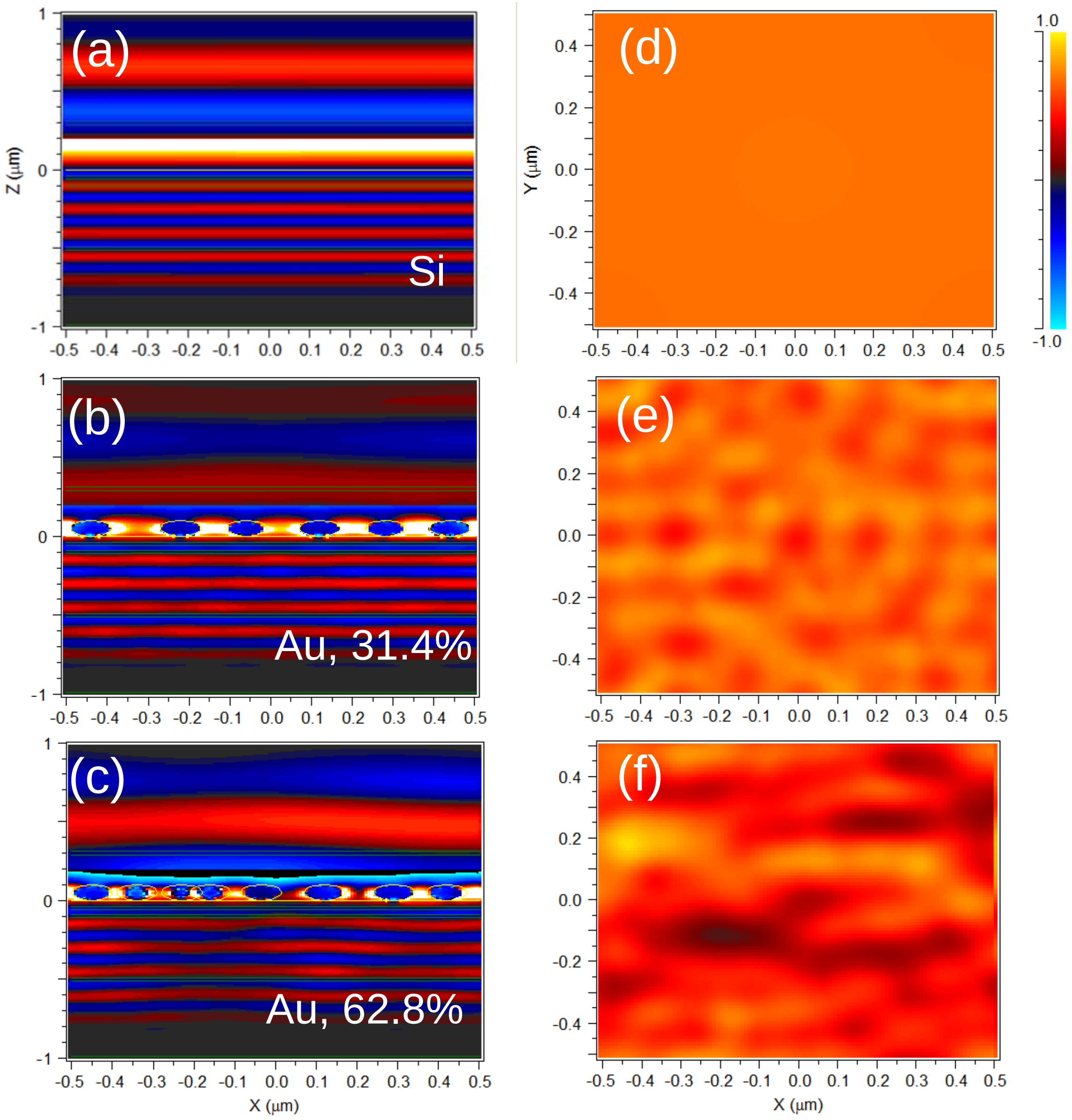

Figure 3. Plane waves propagated from 200 nm above the air–Si interface to the Si substrate in the (a) absence and (b, c) presence of Au NPs at surface coverages of (b) 31.4 and (c) 62.8%. (d)–(f) Images of the X–Y plane at a value of Z of –50 nm, corresponding to (a)–(c), respectively. The colors represent the electric field intensity.

In this case, the reflection curve revealed a distinctive change after depositing the Au NP array (blue line in Figure 4b): the reflection increased at ca. 600 nm and decreased at longer wavelengths ($\lambda > 700$ nm). The transmission curve also features a disproportional trend (blue line in Figure 4c): the transmission decreased at ca. 600 nm and increased at longer wavelengths ($\lambda > 700$ nm). These observations provide additional evidence that the Au NP array was an antireflection layer—because it could not increase the transmission when the reflection was near zero, whereas it could do so when the reflection was nonzero. Previously, we reported an ultralow-reflective Si textured surface featuring close-packed pyramids having dimensions on the subwavelength scale (Chen et al., 2007). Figure 4d provides a schematic representation of a pyramidal textured Si surface having a period of 500 nm and a height of 1000 nm. Because the subwavelength pyramidal structure features a refractive index gradient, its reflection was less than 0.005 over the entire wavelength region (black line in Figure 4e). After coating Au NPs onto the surfaces of the pyramids, the reflection increased dramatically, revealing a maximum peak that was due to scattering from the Au NPs (red line in Figure 4e). In addition, the transmission power decreased in response to the increased reflection after coating the Au NPs (red line in Figure 4f). Interestingly, the increase in reflection (a power difference of ca. 0.14 at 700 nm) was much less than the decrease in transmission (a power difference of ca. 0.6 at 700 nm) because of the absorption of the Au NP array. Clearly, under the ultralow-reflection conditions, the Au NPs scattered (increased reflection) and absorbed (decreased transmission) the incident light.

Next, we experimentally verified the results obtained from the FDTD simulations by using two kinds of Si solar cells: a commercial cell featuring a Si_3N_4 antireflection layer–coated textured surface and a planar cell fabricated using a crystalline Si wafer. We deposited the Au NPs onto the cells that had been exposed to a poly-l-lysine solution, thereby allowing adsorption of the particles on the surfaces (Lim et al., 2007). Figures 5a and 5b display typical SEM images of the commercial textured cell and the planar cell, respectively, after their immersion into Au colloid solutions for 1 h; the two samples had average Au surface coverages of ca. 1.9 and ca. 1.2%, respectively, comparable with those obtained previously (Schaadt et al., 2005; Lim et al., 2007). The inset to Figure 5a provides a higher-magnification SEM image of the Au NPs of uniform size (D = 100 nm) near a peak of the textured surface. Next, we investigated the effect on the photocurrent of the solar cells after depositing the Au NPs arrays. The commercial Si solar cell had an external efficiency of ca. 11%, an open-circuit voltage (V_{oc}) of ca. 0.51 V, and a short circuit current density (J_{sc}) of ca. 35.2 mA cm^{-2} under AM 1.5 filtered illumination. The J–V curves in Figure 5c reveal similar values of V_{oc} but a distinctive drop in J_{sc} (from 35.2 to 16.2 mA cm^{-2}) after coating the particles on the textured surface. These findings indicate that the Au NPs did not affect the photon–electron conversion mechanism, but they strongly reduced the amount of incident light propagating into the cell. We attribute this behavior to the Au NPs disrupting the antireflection abilities of the Si_3N_4 layer and the textured surface (Nagel et al., 1999; Lee et al., 2002) because the particles strongly scattered and absorbed the incident light before it propagated into the cell. Our findings also reveal that the Au NP arrays could not further improve the efficiency of commercial Si solar cells that had been modified with suitable antireflection treatments.

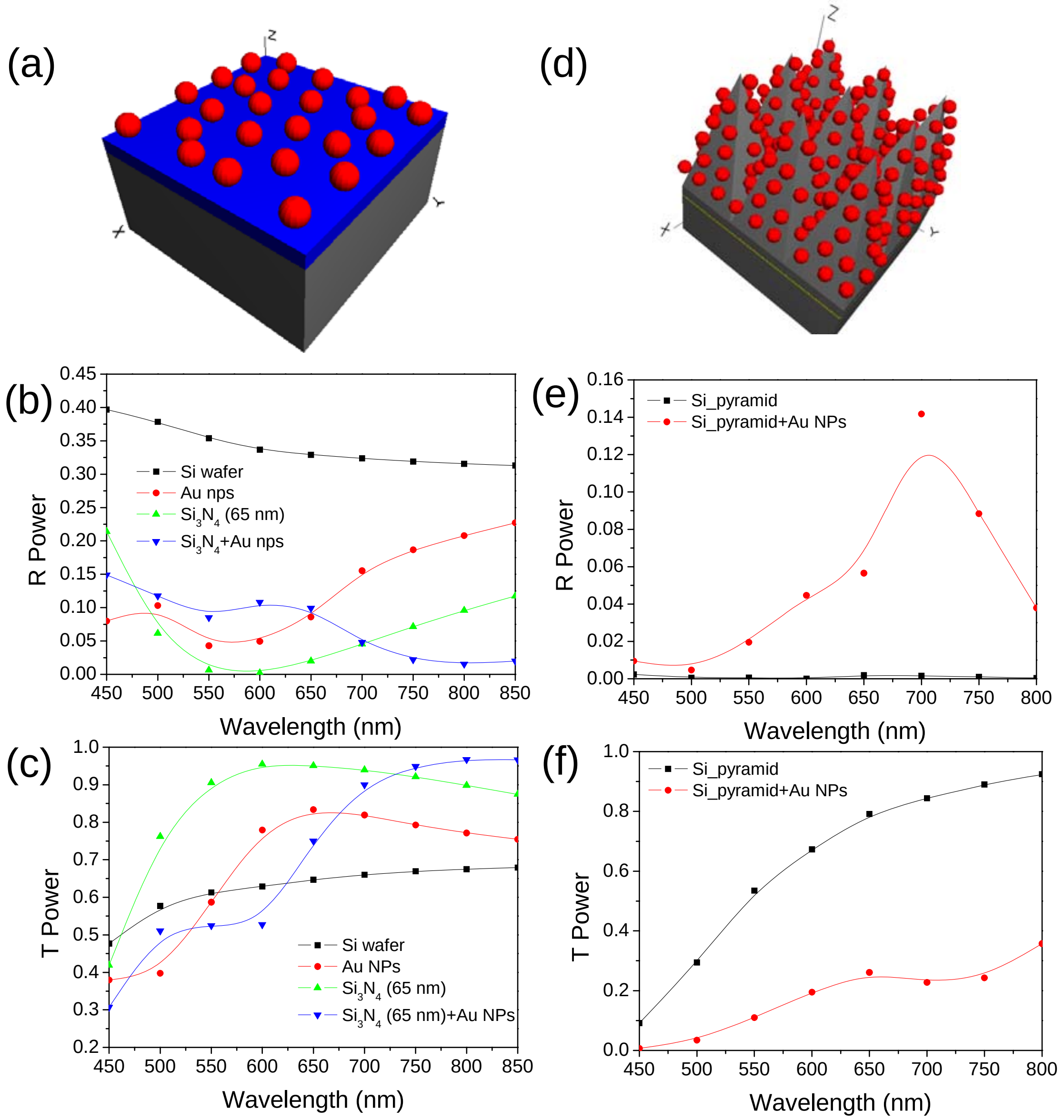

Figure 4. (a) 3D model and (b, c) calculated (b) reflection and (c) transmission spectra of a Si_3N_4 (65 nm)–coated Si substrate in the presence (blue) and absence (green) of a Au NP array. (d) 3D model and (e, f) calculated (e) reflection and (f) transmission spectra of a Si substrate featuring a pyramidal textured surface in the presence (red) and absence (black) of a Au NP array. The period of pyramids was 500 nm; their height was 1000 nm.

Next, we focused on measuring the performance of the planar Si wafer cells that had been used in previously reported SPR-enhanced photodiodes (Schaadt et al., 2005; Lim et al., 2007; Sundararaian et al., 2008). To further examine the antireflection function of the Au NP arrays, it is necessary for us to compare the changes in photocurrents of the devices before and after depositing particles, recorded under two optical conditions: normal incidence (high reflection) and at the Brewster angle (ultralow reflection). Generally, the high reflection of planar Si wafers is attributed to the large difference in the refractive indices of air and Si. Brewster discovered a special phenomenon in the Fresnel reflection of linearly polarized light at large incident angles (Hecht, 2002): when the incoming light has its electric field aligned parallel to the incident plane (i.e., TM-polarized light), its reflected wave will vanish at a certain incident angle known as the Brewster angle. To construct ultralow reflection conditions, we employed TM-polarized light and illuminated our samples at the Brewster angle of a Si wafer (ca. 76° in the visible wavelength regime). Figure 5d displays the photocurrent response of the planar Si solar cell in the presence of Au NPs under TM-polarized illumination at incident angles of 0 and 76°, normalized to the photocurrent response of the planar Si solar cell in the absence of Au NPs. Depending upon the incident angles, the Au NP array had two dramatically different effects on the photocurrent of the planar Si cell. At the normal incident angle (black line in Figure 5d), the Au NP array resulted in a slight, wavelength-dependent increase in photocurrent (ca. 5–10%), consistent with that described in a previous report (Lim et al., 2007). In contrast, the Au NPs strongly suppressed the photocurrent over the entire wavelength region when we illuminated the sample under TM-polarized light at the Brewster angle (76°, red line in Figure 5d). These results indicate that the Au NP array could not increase the photocurrent of the solar cells through the scattering of reflected light into the cells when no light was reflected from the air–Si interface under these specific conditions. In addition, the Au NP array also absorbed the incoming light and then suppressed the photocurrent of the cells. Of course, solar cells would not be used under these specific conditions, but this particular phenomenon provides powerful evidence supporting our assumption that the photocurrent enhancement of the Si wafer cells resulted from the antireflection ability of the Au NP array. Based on the simulated and experimental results, we suggest that a monolayer Au NP array should be considered as an absorbed antireflection layer. Compared with other routine methods for the preparation of antireflection Si solar cells, such as the use of antireflection coatings (Nagel et al., 1999; Lee et al., 2002) and the formation of textured surfaces through dry- or wet-etching (Winderbaum et al., 1997; Macdonald et al., 2004; Chen et al., 2007), the solution-based processing that we used to fabricate our monolayer Au NP arrays has several advantages: (i) it is a simple, rapid, and economical fabrication method that does not require any expensive equipment; (ii) it does not destroy the substrate surface or the buried p–n junction; and (iii) it can be performed using single-crystalline, multi-crystalline, and amorphous Si substrates. Nevertheless, the one apparent disadvantage of this approach—the intrinsic absorption of the metal NPs—must be overcome if it is to be used in practical devices. In an attempt to solve this problem, we replaced the metal NPs with dielectric NPs (i.e., SiO_2 and TiO_2), which are generally transparent in the visible and near-infrared regimes.

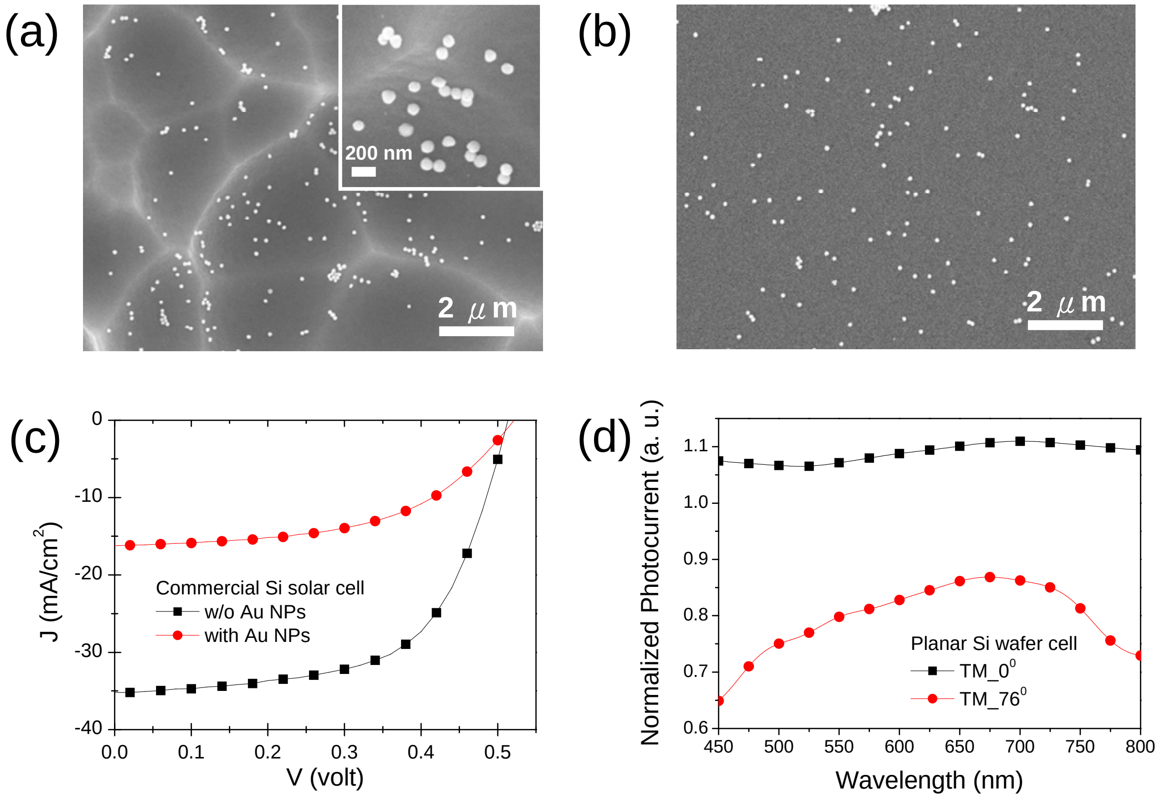

Figure 5. (a, b) Top-view SEM images of (a) a commercial Si cell and (b) a planar Si cell loaded with Au NPs for 1 h. Inset: Higher-magnification SEM image corresponding to (a). (c) Current density–voltage curves for the commercial Si cell in the presence (red) and absence (black) of a Au NP array. (d) Normalized photocurrent spectra of the Au NP–coated planar Si photodiode, recorded under TM-polarized illumination at incident angles of 0° (black) and 76° (Brewster angle, red).

To examine the performance of the dielectric NP–coated Si substrates, we employed the same simulation model as that used to obtain Figure 1a, with the optical constants of the dielectric materials (n_{SiO2} = 1.46 and n_{TiO2} = 2.75 at 600 nm) obtained from the literature (Palik, 1985). Figures 6a and 6b present the calculated total reflection and transmission power spectra, respectively, of Si substrates in the absence and presence of SiO_2 and TiO_2 NP arrays at a surface coverage of 19.6%. Both arrays effectively reduced the amount of reflected light from the Si surface and uniformly increased the transmission power over the entire wavelength regime. Notably, the latter optical phenomenon of the dielectric NPs was very different from that of the Au NPs, which generally suppressed transmission at short wavelengths (see Figure 2a). In addition, the TiO_2 NPs exhibited better antireflection ability (e.g., a decrease from 0.33

to 0.23 at 600 nm) than did the SiO_2 NPs (e.g., from 0.33 to 0.30 at 600 nm) and, therefore, they could more efficiently increase the amount of light transmitted into the substrate (e.g., from 0.63 to 0.74 at 600 nm). Next, we controlled the surface coverage and diameter of the TiO_2 NPs to optimize the transmission power. Upon increasing the coverage from 19.6 to 62.8%, the maximum of transmission power (Figure 6c) increased from 0.75 (λ = 650 nm; cyan line) to 0.94 (λ = 650 nm; red line). The highest transmission power (0.97 at 850 nm) occurred when we deposited the TiO_2 NP array into a close-packed monolayer (pink line in Figure 6c). Furthermore, we observed a blue-shift in the peak transmission power of the close-packed TiO_2 NP arrays toward visible wavelengths upon decreasing the average diameter of the particles from 100 to 50 nm (see Figure 6d). Finally, we found that the optimized transmission power, relative to the AM 1.5 solar spectrum, resulted from close-packed TiO_2 NPs having an average diameter of 65 nm (Cole and Halas, 2006). Besides, the optimized TiO_2 NPs (65 nm) display a more significant antireflection ability when compared with that of the thin TiO_2 film having an optimized thickness of ca. 48 nm (hollow circle in Figure 6d). The performance of the TiO_2 NPs was superior to that of the Au NPs because they provided greater reflection and increased transmission over the entire wavelength region without any absorption loss.

Figure 7 presents the behavior of a plane wave having a wavelength of 600 nm propagated from 200 nm above the air–Si interface to Si surfaces featuring sparse coverages (19.6%) of dielectric NPs (SiO_2 and TiO_2) or close-packed TiO_2 NPs. Compared with the behavior of the Si surface in the absence of particles (Figure 3a), Figure 7a reveals that the plane wave propagating to the air–Si surface in the presence of a sparse coverage of SiO_2 NPs (D = 100 nm) exhibited a slightly reduced reflection electric field above the Si surface. A weaker reflection field existed when the plane wave propagated to the dispersed TiO_2 NP array (D = 100 nm; Figure 7b); more parts of the propagating wave were distributed in the Si substrate. For the close-packed TiO_2 NP array (D = 65 nm), only a quite weak wave existed above the Si substrate, due to the optimized antireflection properties (Figure 7c). Therefore, the amount of reflected light in the near field was reduced dramatically when employing a close-packed array of TiO_2 NPs having an optimized average diameter (i.e., 65 nm). To further investigate the optical behavior of transmitted plane waves, Figures 7d–f present the electric field distributions of the X–Y planes at a value of Z of –50 nm, corresponding to the models used in Figures 7a–c, respectively. Compared with the weak electric field in the Si substrate in the absence of particles (Figure 3d), Figures 7d–f display a series of sequentially brighter images. Note that the images of the surfaces featuring the dielectric NPs (sparsely or closely packed particles) are brighter throughout, rather than exhibiting randomly distributed regions of brightness arising from the Au NP arrays (cf. the presence of some darker regions in Figure 3f). We attribute this behavior to the dielectric NPs not causing any absorption loss.

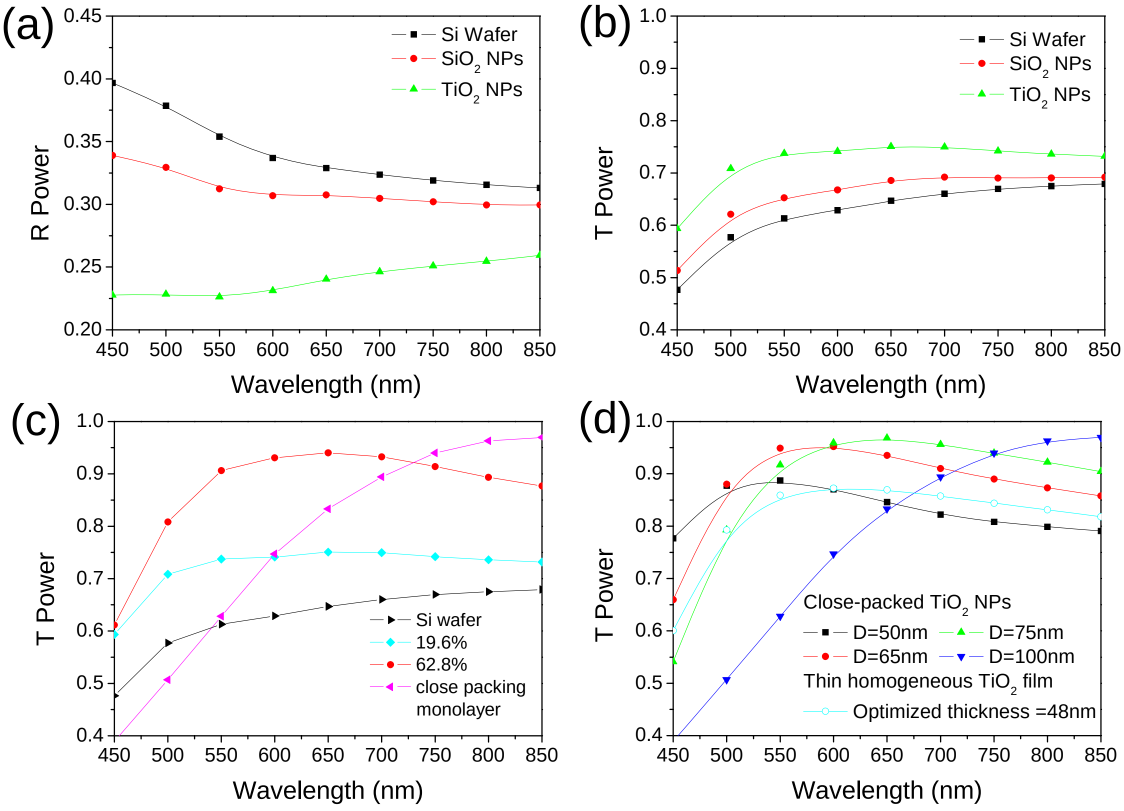

Figure 6. (a, b) Calculated (a) reflection and (b) transmission spectra of Si substrates in the absence (black) and presence of SiO_2 NP (red) and TiO_2 NP (green) arrays (surface coverage: 19.6%). (c) Calculated transmission spectra of Si substrates in the absence (black) and presence of TiO_2 NP arrays having surface coverages of 19.6% (cyan) and 62.8% (red) and a close-packed TiO_2 NP monolayer (pink). (d) Calculated transmission spectra of Si substrates covered with a thin TiO_2 film (hollow circle) and close-packed arrays of TiO_2 NPs having average diameters of 50, 65, 75, and 100 nm.

To study the antireflection behavior of the dielectric NP arrays, we employed the effective medium theory (Knittl, 1976) and considered the principle of a single layer antireflection coating.(Hecht 2002) We presumed that our monolayer NP arrays were thin films having a thickness equal to the diameter of the particles and then calculated the effective refractive index (n_{eff}) of the thin film according to the effective medium model. The extinction coefficients of the dielectric NPs could be neglected in the considered wavelength range.

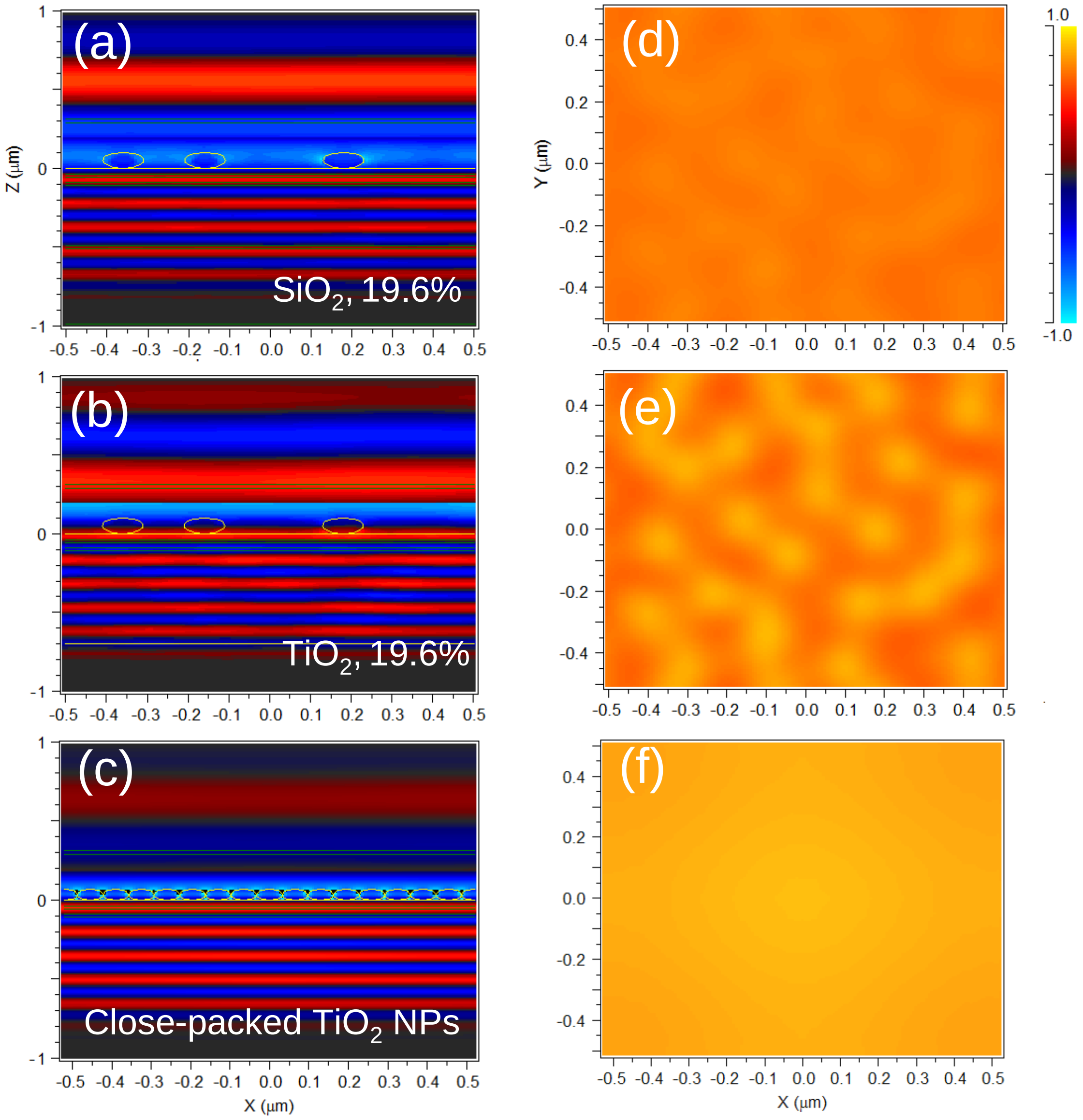

Figure 7. (a)–(c) Plane waves propagated from 200 nm above the air–Si interface to Si substrates presenting (a) SiO_2 NPs (D = 100 nm) and (b) TiO_2 NPs (D = 100 nm) at surface coverages of 19.6% and (c) close-packed TiO_2 NPs (D = 65 nm). (d)–(f) Images of the X–Y plane at a value of Z of –50 nm, corresponding to (a)–(c), respectively. The colors represent the electric field intensity.

For example, the SiO_2 and TiO_2 dielectric NP arrays had values of n_{eff} of 1.06 and 1.23, respectively, when the surface coverage was 19.6% (V_{NP} = 13%) and the wavelength was 600 nm. According to the well-established equation (Hecht, 2002)

$$n_{ARC} = \sqrt{n_{air} n_{Si}} \qquad (1)$$

a single layer antireflection coating on Si (n_{Si} = 3.94 at 600 nm) should have a value of n_{ARC} of ca. 1.98. Therefore, we would expect the TiO_2 NP array ($n_{\mathrm{eff}} = 1.23$) to reduce the amount of reflected light to a greater degree than would the SiO_2 NP array ($n_{\mathrm{eff}} = 1.06$) because the value of n_{eff} of the TiO_2 NP array is closer to 1.98 (see Figure 6a). Moreover, we could increase the value of n_{eff} of the TiO_2 NP array from 1.23 to 1.73 by increasing the surface coverage from 19.6% ($V_{\mathrm{NP}} = 13\%$) to 62.8% ($V_{\mathrm{NP}} = 42\%$), as indicated in Figure 6c. As expected, the close-packed TiO_2 NP array ($V_{\mathrm{NP}} = 60\%$) having a value of n_{eff} of 2.06 (close to 1.98) provided the highest transmission power (Figure 6c). In addition, it also explained that the close-packed TiO_2 NPs exhibit a better antireflection ability than a thin TiO_2 film dose. The blue-shift of the transmission peaks in Figure 6d could be explained by considering that the lowest degree of reflection would exist at the specific wavelength according to the equation (Hecht, 2002)

$$\frac{1}{4}\lambda_{\mathrm{dip}} = \mathrm{n}_{\mathrm{ARC}}\mathrm{D} \tag{2}$$

where D is the thickness of the antireflection layer, equal to the average diameter of the TiO_2 NPs. Therefore, a decrease in the wavelength of the lowest reflection (λ_{dip}) accompanied the blue-shift of the transmission peaks upon decreasing the diameter of the particles (Figure 6d). Notably, although Matheu et al. (2008), and Sundararaian et al. (2008), both reported photocurrent enhancements from sparse coverages (<15%) of SiO_2 NP arrays, they focused only on the scattering properties of the particles, omitting the important antireflection properties of their arrays. Thus, they only obtained small increases in photocurrent (<10%), whereas we predicted increases of greater than 30% when employing the optimized TiO_2 NP array. In addition, some previous groups utilized close-packed SiO_2 NPs as antireflective coatings for glass (Nostell et al., 1999; Rouse and Ferguson, 2003; Hattori, 2001; Prevo et al., 2005; Prevo et al., 2007) or Si (Prevo et al., 2007) substrates. As expected, they only reduced partial reflection of the air－Si surfacealthough they succeeded reducing most of reflection of the air－glass surface due to the low refractive index of silica. In other words, TiO_2 NPs exhibiting higher refractive index might be a more suitable candidate for the antireflective coatings for Si solar cells.

Moreover, we experimentally investigated the antireflection behavior of a close-packed TiO_2 NP layer for planar Si solar cells. In general, TiO_2 films are commonly prepared using physical [i.e., sputtering (Dholam et al., 2008), chemical vapor deposition (Borras et al., 2009)] and chemical[i.e., sol–gel (Harizanov and Harizanova, 2000)] methods. In this study, we developed a simple, rapid, and economical solution-based method for fabricating close-packed TiO_2 NP thin films atop Si wafers; this process can be performed at room temperature under atmospheric pressure without requiring any post-annealing treatment (typically >500 °C for sol–gel processing) or expensive instrumentation (generally necessary for physical deposition processes). First, we diluted a commercially available TiO_2 dispersion solution to 4.68 wt% with ethanol and then spin-coated it onto the Si wafers. The spin-coating method was similar with that performed to fabricate close-packed SiO_2 NPs layers by Jiang et al.,[42] The dispersion of crystalline TiO_2 (20% rutile, 80% anatase) featured particles having sizes of less than 100 nm, with the primary particle size being ca. 15 nm. Tuning the spin-coating rate allowed us to readily control the optical properties and thicknesses of the TiO_2 NP thin films. Figure 8a presents the reflectance spectra of Si wafers in the absence and presence of TiO_2 NP films deposited at various spinning rates. After spin-coating the TiO_2 NP films, the reflectance of the substrate decreased dramatically from 35% to less than 15% over the entire wavelength region. In particular, the reflectance was less than 5% within a wavelength range from 500 to 600 nm, the major component of the AM 1.5 solar spectrum (Cole and Halas, 2006). For example, the sample prepared at 5900 rpm exhibited its lowest reflectance of 0.27% at 547 nm (green line in Figure 8a).

Next, we obtained the effective refractive index (n_{eff}) and thicknesses of the close-packed TiO_2 NP films through fitting of the reflectance spectra and the estimated thicknesses determined from SEM cross-sectional images of the samples. The detailed fitting method has been described elsewhere (Hecht, 2002; Wan et al., 2009). Figure 8b displays the values of n_{eff} at 600 nm and the thicknesses of the TiO_2 NPs films prepared at various spinning rates. Upon increasing the spinning rate from 5000 to 8000 rpm, the films decreased in thickness from 72 to 61 nm, while their values of n_{eff} remained similar (only a slight increase from 1.97 to 2.11). The decreased thickness resulted in a blue-shift of the reflectance dip in Figure 8a, as predicted from the equation above. Notably, the values of n_{eff} were close to the optimized value of 1.98 (λ = 600 nm) expected for an antireflection coating on a Si wafer. Besides, the values of the volume fraction (V_{NP}) of TiO_2 NPs were estimated through the effective medium model. For instance, the V_{NP} of ca. 70% was estimated based on the n_{eff} of 1.97 (5000 rpm, $\lambda = 600$ nm) and the n_{TiO2} of 2.4 (purchased particles, 20% rutile, 80% anatase). The value was slightly higher than the value ($V_{NP} = 60\%$) calculated by geometry. The reason could be attributed to that some smaller particles might fill the space between the larger TiO_2 NPs. Finally, we prepared a close-packed TiO_2 NP film atop a planar Si solar cell to induce an increased photocurrent in the cell.

Figure 8c presents the photocurrent response of a planar Si solar cell after spin-coating the TiO_2 NP film at 5900 rpm, normalized with respect to the photocurrent response of the corresponding cell in the absence of TiO_2 NPs. These spectra were recorded under unpolarized illumination at normal incident angle. The TiO_2 NP–coated cell exhibited a ca. 30% increase in photocurrent over the entire wavelength region, in good agreement with our simulated optimization (see Figure 6)—although slightly lower because of scattering reflection loss. The uniform photocurrent enhancements over the entire visible wavelength region indicate that the use of dielectric NPs allowed us to overcome the problems associated with the SPR absorptions of metal NPs. To the best of our knowledge, this uniform photocurrent enhancement is greater than those obtained from previously reported metal and dielectric NP–enhanced Si wafer-based solar cells (Lim et al., 2007; Pillai et al., 2007; Hagglund et al., 2008; Matheu et al., 2008; Sundararaian et al., 2008). In addition, we suspect that this solution-based technique for preparing dielectric NP antireflection coatings could be further extended to devices featuring surface materials of various refractive indices, such as GaAs, indium tin oxide (ITO), and ZnO. For example, we might employ close-packed TiO_2 NP films for GaAs surfaces (n = 3.91; n_{ARC} = 1.98) or close-packed polystyrene NP films (n = 1.59; n_{eff} = 1.36) for ITO surfaces (n = 1.88; n_{ARC} = 1.37).

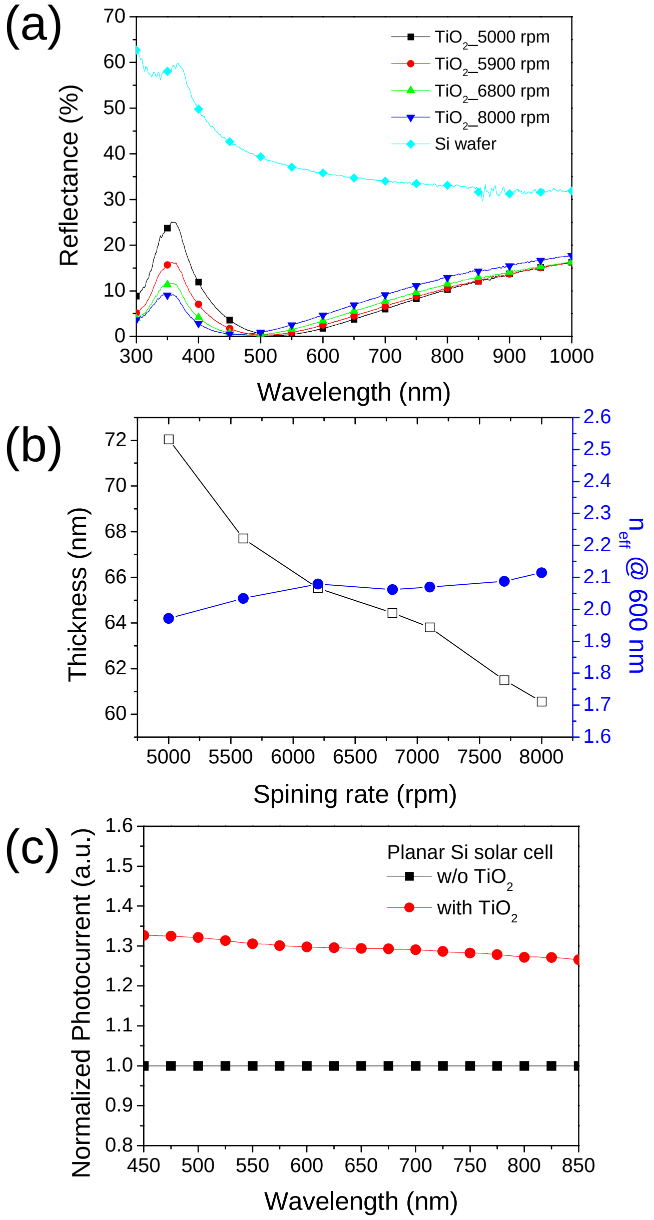

Figure 8. (a) Reflectance spectra of Si wafers before and after spin-coating a film of close-packed TiO_2 NPs at various spinning rates. (b) Thickness (square) and effective refractive index (n_{eff}) at a wavelength of 600 nm (circle) of the close-packed TiO_2 NP films, plotted with respect to the spin-coating rate. (c) Normalized photocurrent spectra of the TiO_2 NP–coated planar Si cells, recorded under unpolarized illumination at normal incident angle.

4. Conclusions

We have systematically investigated the mechanism through which NP arrays induce photocurrent enhancements in Si-based solar cells. First, we used the three-dimensional FDTD method to analyze the optical behavior in the near field regime of a monolayer Au NP array deposited on a Si substrate at various surface coverages. Based on the calculated total transmission and reflection spectra, we found that the transmission power increased at longer wavelengths upon increasing the Au NP surface coverage, whereas it decreased dramatically at wavelengths of less than 550 nm. We attribute the increases in transmission to the decreased reflection of the Si substrates resulting from forward scattering of the Au NPs. Notably, however, an apparent dip ($\lambda <$ 550 nm) in the transmission power curves was due to the intrinsic absorption of Au NPs. Hence, we suspected that our Au NP arrays acted as deficient single-layer antireflection coatings: they could reduce the amount of reflected light, scattering it into the Si substrates, while strongly absorbing the incident light at SPR wavelengths. Most importantly, the unavoidable absorption loss generally covered the maximum power peak of the AM 1.5 solar spectrum. Next, we used the FDTD simulations to demonstrate the failure of the transmission enhancement by positioning Au NP arrays atop Si substrates possessing ultralow reflection surfaces: either a single layer of a Si_3N_4 antireflection film or a pyramidal textured structure. In addition, we also experimentally demonstrated the strong suppression of the photocurrents of two kinds of the Si solar cells: a commercial textured cell with a Si_3N_4 antireflection coating and a planar cell (recorded at the Brewster angle). The calculated and experimental results obtained under ultralow-reflection conditions strongly supported our assumption regarding the role of the Au NPs. Moreover, we used dielectric NPs as antireflection coating materials to overcome the problems associated with the SPR absorptions of the metal NPs. In FDTD simulations, we controlled the surface coverage and diameter of these particles to optimize their antireflection ability. We found that a close-packed array of TiO_2 NPs having a diameter of 65 nm and a effective refractive index of ca. 2.06 displayed uniformly high transmission power over the entire wavelength regime (e.g., 0.95 at 550 nm)—much better than that obtained from the Au NP arrays. Finally, we developed a solution-based method to form close-packed crystalline TiO_2 NP thin films atop planar Si wafer solar cells without requiring any post-annealing treatment or expensive equipment. Tuning the spin-coating rate allowed us to readily control the thickness and effective refractive index of the TiO_2 NP films; we obtained an optimized antireflection coating that provided a uniform ca. 30% increase in photocurrent over the entire wavelength region. Furthermore, this solution-based technique for preparing dielectric NP antireflection coatings has great potential for improving the performance of various other devices that feature surface materials having different refractive indices, such as GaAs, ITO, and ZnO.

References

Akimov, Y. A., W. S. Koh, et al., 2009. Enhancement of optical absorption in thin-film solar cells through the excitation of higher-order nanoparticle plasmon modes, Optics Express, 17(12), 10195-10205.

Borras, A., J. R. Sanchez-Valencia, et al., 2009. Growth of Crystalline TiO_2 by Plasma Enhanced Chemical Vapor Deposition, Crystal Growth & Design, 9(6), 2868-2876.

Catchpole, K. R. and A. Polman, 2008. Design principles for particle plasmon enhanced solar cells, Applied Physics Letters, 93(19), 191113.

Catchpole, K. R. and A. Polman, 2008. Plasmonic solar cells, Optics Express, 16(26), 21793-21800.

Chen, H. L., S. Y. Chuang, et al., 2007. Using colloidal lithography to fabricate and optimize sub-wavelength pyramidal and honeycomb structures in solar cells, Optics Express, 15(22), 14793-14803.

Cole, J. R. and N. J. Halas, 2006. Optimized plasmonic nanoparticle distributions for solar spectrum harvesting, Applied Physics Letters, 89(15), 153120.

Dholam, R., N. Patel, et al., 2008. Physically and chemically synthesized TiO2 composite thin films for hydrogen production by photocatalytic water splitting, International Journal of Hydrogen Energy, 33(23), 6896-6903.

Duche, D., P. Torchio, et al., 2009. Improving light absorption in organic solar cells by plasmonic contribution, Solar Energy Materials and Solar Cells, 93(8), 1377-1382.

Hagglund, C., M. Zach, et al., 2008. Electromagnetic coupling of light into a silicon solar cell by nanodisk plasmons, Applied Physics Letters, 92(5), 053110.

Hallermann, F., C. Rockstuhl, et al., 2008. On the use of localized plasmon polaritons in solar cells, Physica Status Solidi a-Applications and Materials Science, 205(12), 2844-2861.

Harizanov, O. and A. Harizanova, 2000. Development and investigation of sol-gel solutions for the formation of TiO2 coatings, Solar Energy Materials and Solar Cells, 63(2), 185-195.

Hecht, E., 2002. *Optics*, Addison-Wesley.

Kelly, K. L., E. Coronado, et al., 2003. The optical properties of metal nanoparticles: The influence of size, shape, and dielectric environment, Journal of Physical Chemistry B, 107(3), 668-677.

Khlebtsov, B. N., V. A. Khanadeyev, et al., 2008. Coupled plasmon resonances in monolayers of metal nanoparticles and nanoshells, Physical Review B, 77(3).

Khurgin, J. B., G. Sun, et al., 2009. Practical limits of absorption enhancement near metal nanoparticles, Applied Physics Letters, 94(7), 071103.

Kim, S. S., S. I. Na, et al., 2008. Plasmon enhanced performance of organic solar cells using electrodeposited Ag nanoparticles, Applied Physics Letters, 93(7), 073307.

Knittl, Z. E., 1976. *Optics of thin films; an optical multilayer theory*, New York, Wiley.

Lee, S. H., I. Lee, et al., 2002. Silicon nitride films prepared by high-density plasma chemical vapor deposition for solar cell applications, Surface & Coatings Technology, 153(1), 67-71.

Lim, S. H., W. Mar, et al., 2007. Photocurrent spectroscopy of optical absorption enhancement in silicon photodiodes via scattering from surface plasmon polaritons in gold nanoparticles, Journal of Applied Physics, 101(10), 104309.

Macdonald, D. H., A. Cuevas, et al., 2004. Texturing industrial multicrystalline silicon solar cells, Solar Energy 76(1-3), 277-283.

Matheu, P., S. H. Lim, et al., 2008. Metal and dielectric nanoparticle scattering for improved optical absorption in photovoltaic devices, Applied Physics Letters, 93(11), 113108.

Nagel, H., A. G. Aberle, et al., 1999. Optimised antireflection coatings for planar silicon solar cells using remote PECVD silicon nitride and porous silicon dioxide, Progress in Photovoltaics, 7(4), 245-260.

Palik, E. D., 1985. *Handbook of optical constants of solids*, Orlando, Academic Press.

Pillai, S., K. R. Catchpole, et al., 2007. Surface plasmon enhanced silicon solar cells, Journal of Applied Physics, 101(9), 093105.

Schaadt, D. M., B. Feng, et al., 2005. Enhanced semiconductor optical absorption via surface plasmon excitation in metal nanoparticles, Applied Physics Letters, 86, 063106.

Sundararaian, S. P., N. K. Grady, et al., 2008. Nanoparticle-induced enhancement and suppression of photocurrent in a silicon photodiode, Nano Letters, 8(2), 624-630.

Wan, D. H., H. L. Chen, et al., 2008. Using Self-Assembled Nanoparticles to Fabricate and Optimize Subwavelength Textured Structures in Solar Cells, Journal of Physical Chemistry C, 112(51), 20567-20573.

Wan, D. H., H. L. Chen, et al., 2009. Using Spectroscopic Ellipsometry to Characterize and Apply the Optical Constants of Hollow Gold Nanoparticles, ACS Nano, 3(4), 960-970.

Winderbaum, S., O. Reinhold, et al., 1997. Reactive ion etching (RIE) as a method for texturing polycrystalline silicon solar cells, Solar Energy Materials and Solar Cells, 46(3), 239-248.